SOLAR CELLS

# Highly efficient p-i-n perovskite solar cells that endure temperature variations

Guixiang Li[1]†, Zhenhuang Su[2]†, Laura Canil[1], Declan Hughes[3], Mahmoud H. Aldamasy[1], Janardan Dagar[1], Sergei Trofimov[1], Luyao Wang[1]*, Weiwei Zuo[4], José J. Jerónimo-Rendon[4], Mahdi Malekshahi Byranvand[4,5], Chenyue Wang[2], Rui Zhu[6], Zuhong Zhang[6], Feng Yang[6], Giuseppe Nasti[7], Boris Naydenov[1], Wing C. Tsoi[3], Zhe Li[8], Xingyu Gao[2], Zhaokui Wang[9], Yu Jia[6], Eva Unger[1], Michael Saliba[4,5], Meng Li[1,6,8]*, Antonio Abate[1,7]*

Daily temperature variations induce phase transitions and lattice strains in halide perovskites, challenging their stability in solar cells. We stabilized the perovskite black phase and improved solar cell performance using the ordered dipolar structure of β-poly(1,1-difluoroethylene) to control perovskite film crystallization and energy alignment. We demonstrated p-i-n perovskite solar cells with a record power conversion efficiency of 24.6% over 18 square millimeters and 23.1% over 1 square centimeter, which retained 96 and 88% of the efficiency after 1000 hours of 1-sun maximum power point tracking at 25° and 75°C, respectively. Devices under rapid thermal cycling between −60° and +80°C showed no sign of fatigue, demonstrating the impact of the ordered dipolar structure on the operational stability of perovskite solar cells.

The highest power conversion efficiencies (PCEs) of >25% reported for single-junction perovskite solar cells (PSCs) rely on regular n-i-p architectures (*1*). However, inverted p-i-n PSCs have several advantages, including low-temperature processability and long-term operational stability derived from non-doped hole-transporting materials (*2*, *3*). Nonetheless, they have lower PCEs, with only a few certified values exceeding 23% and a bottleneck value of 24% over 10 square millimeter cells (*4*–*6*). This lower performance is mainly correlated with nonradiative recombination losses and reduced charge extraction that stem from the high density of defects in the perovskite bulk and interfacial contacts (*7*, *8*).

[1]Helmholtz-Zentrum Berlin für Materialien und Energie GmbH, Hahn-Meitner-Platz 1, 14109 Berlin, Germany. [2]Shanghai Synchrotron Radiation Facility (SSRF), Shanghai Advanced Research Institute, Chinese Academy of Sciences, 239 Zhangheng Road, Shanghai 201204, China. [3]SPECIFIC, Department of Materials Science and Engineering, Faculty of Science and Engineering, Swansea University, Bay Campus, Fabian Way, Swansea SA1 8EN, UK. [4]Institute for Photovoltaics (*ipv*), University of Stuttgart, Pfaffenwaldring 47, D-70569 Stuttgart, Germany. [5]Helmholtz Young Investigator Group FRONTRUNNER, IEK5-Photovoltaics, Forschungszentrum Jülich, 52425 Jülich, Germany. [6]Key Lab for Special Functional Materials of Ministry of Education, National & Local Joint Engineering Research Center for High-efficiency Display and Lighting Technology, School of Materials Science and Engineering, Collaborative Innovation Center of Nano Functional Materials and Applications, Henan University, Kaifeng 475004, China. [7]Department of Chemical, Materials and Production Engineering, University of Naples Federico II. Naples, pzz.le Vincenzo Tecchio 80, 80125 Naples, Italy. [8]School of Engineering and Materials Science (SEMS), Queen Mary University of London, London E1 4NS, UK. [9]Institute of Functional Nano & Soft Materials (FUNSOM), Jiangsu Key Laboratory for Carbon-Based Functional Materials & Devices, Soochow University, Suzhou 215123, China.
***Corresponding author. Email: mengli@henu.edu.cn (M.L.); luyao.wang@helmholtz-berlin.de (L.W.); antonio.abate@helmholtz-berlin.de (A.A.)**
†These authors contributed equally.

For practical applications, ambient temperature variations can limit PSC performance (*9*) because the perovskite can undergo severe ion migration, phase transition, and temperature-induced strain, leading to lower PCE (*10*–*12*). Cycling over variable temperatures demands that the perovskite tolerate alternating tension and compression in the device structure (*13*). Thus, developing high-efficiency PSCs with thermal cycle stability is critical to advancing PSC application.

We use polymer dipoles to optimize triple cation halide perovskite $Cs_{0.05}(FA_{0.98}MA_{0.02})_{0.95}Pb(I_{0.98}Br_{0.02})_3$ films from bulk to the surface. The polymer dipole promoted the growth of a low-defect crystalline film by reducing the formation energy of the black photoactive phase. The formation of dipoles at the perovskite surface suppressed ion migration and facilitated interfacial charge extraction while enhancing hydrophobicity. We achieved a certified PCE of 24.2% over an active area of 9.6 $mm^2$, and lab recorded PCEs of 24.6% over 18 $mm^2$ and 23.1% over 1 $cm^2$. The high PCE was stable under severe thermal cycling (120 cycles, from −60° to +80°C), demonstrating the resiliency of the crystal structure to the temperature-induced strains.

## Film formation and characterization

The alternate symmetric hydro and fluorocarbon units along the polymeric backbone of β-poly(1,1-difluoroethylene) (β-pV2F) result in an ordered molecular dipole distribution. After screening a few molecular weights, 0.5 mg/mL β-pV2F of 180,000 molecular weight was used (figs. S1 and S2). The influence of β-pV2F on the film morphology and work function is shown in Fig. 1. From the top view and cross sectional scanning electron microscope (SEM) images (Fig. 1, A to C), we can observe evident voids at the grain boundaries of the control perovskite film, with an average g size of ~400 nm (fig. S3A). These defects create shunting paths and nonradiative recombination centers (*14*). β-pV2F enabled a more compact perovskite film with an enlarged grain size of ~480 nm (Fig. 1, D to F, and fig. S3B). A smaller full width at half maximum in the (001) peak of the x-ray diffraction support an enhanced crystallinity in the β-pV2F–treated perovskite film (fig. S4) (*15*). Furthermore, atomic force microscopy images showed that β-pV2F reduced the surface roughness from 54.4 to 41.1 nm (fig. S5), which is expected to ameliorate coverage with charge-transporting layers (*16*).

Because of the electron-withdrawing effect of the fluorine atoms, the neighboring hydrogen atoms have a partial positive charge density. Then, the all-trans planar zigzag conformation of β-pV2F makes it resemble a Lewis acid, which can interact with the surface of the perovskite (*17*, *18*). Fourier transform infrared spectroscopy revealed that the $-CH_2$ stretching vibration peak shifted from 3025 $cm^{-1}$ of β-pV2F to 3019 $cm^{-1}$ in contact with the target perovskite (fig. S6), suggesting a solid C-H···X dipole interaction between $-CH_2$ moieties and halide ions of the $[PbX_6]^{4-}$ frame. Such polar interaction with the precursors of the perovskite influences the crystallization during film formation and leads to an upward shift of the surface work function (WF) after film formation (Fig. 1G) (*17*, *18*); Fig. 1H displays the increase in WF up to 300 meV for the target perovskite film, which facilitates the interfacial charge extraction and enhances the device's stability (*19*).

The WF shift was near that of standard perovskite film treated with β-pV2F only at the surface, which indicated that as the crystal growth proceeded, β-pV2F was partially expelled from the bulk and assembled on the perovskite surface (*2*, *20*). The fluorine-exposed surface arrangement induced hydrophobicity (figs. S7 and S8). We measured reduced nonradiative recombination and improved interfacial charge transfer in target perovskites (figs. S9 to S13) (*21*–*24*). This scenario is expected to enhance the solar cells' efficiency and stability (*25*, *26*).

To acquire an in-depth perspective on the promoted perovskite crystallization kinetics, we performed synchrotron-based in situ grazing incidence wide-angle x-ray scattering (GIWAXS) measurements to monitor the entire film formation process (several different stages are shown in Fig. 2, A and B). The initial $t_1$ stage (during the first 25 s) revealed the scattering halo at scattering vector $q$ values from 8 to 8.5 $nm^{-1}$ from the solvated colloidal sol precursor. The signal transition at $t_2$ (25 s) originated from dripping antisolvent, where the rapid solvent extraction caused the disappearance of the diffraction signal. Subsequently,

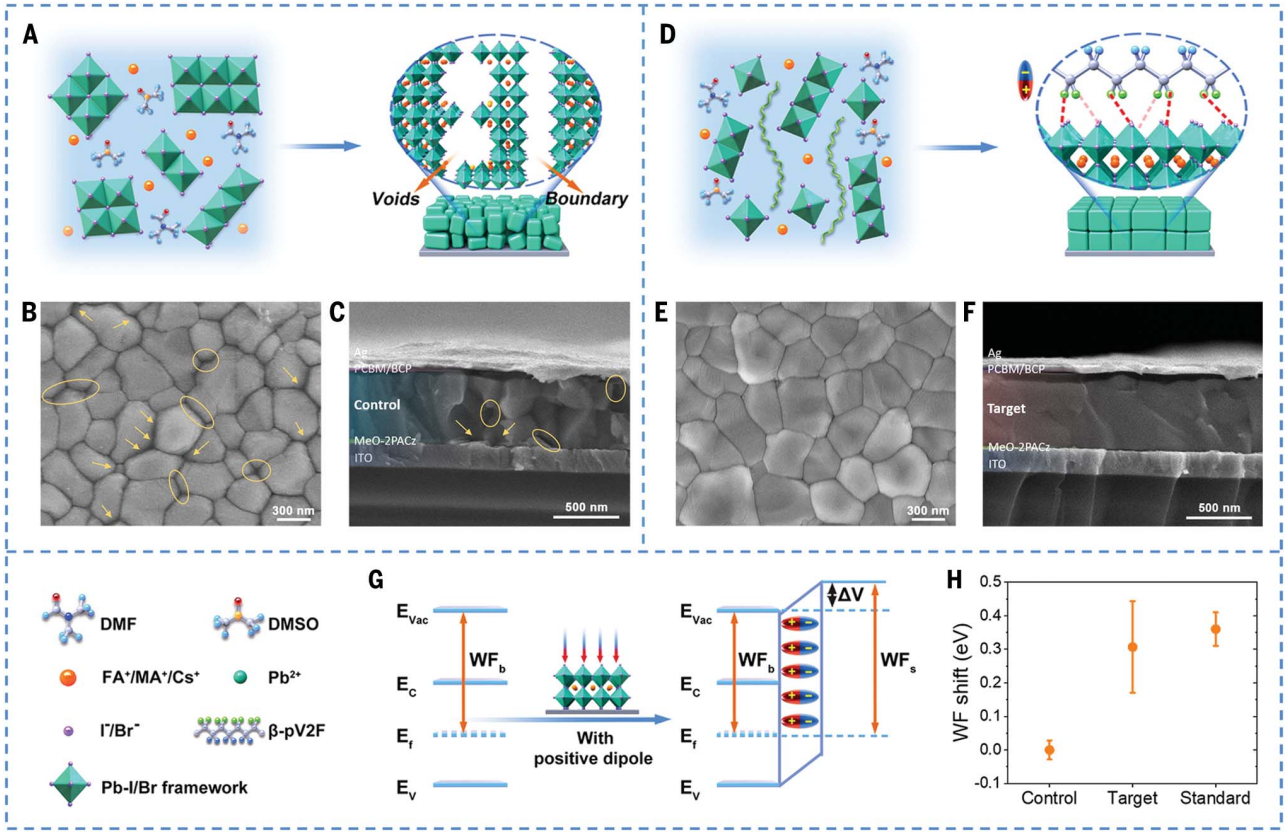


**Fig. 1. Working mechanism and morphology characterization of perovskite films.** Schematic of processing (**A**) control and (**D**) target perovskites. (**B**) Top view and (**C**) cross sectional SEM images of control perovskites. (**E**) Top view and (**F**) cross sectional SEM images of target perovskites. (**G** and **H**) WF shift related to perovskite functionalized with β-pV2F.

the spin coating process was performed at stage $t_3$, where supersaturated solvate intermediate emerges. The $t_4$ near 60 s represented annealing staging. Stage $t_5$ revealed the intermediate phase signal with annealing. Stage $t_6$ was the perovskite evolution process. Stage $t_7$ described the cessation of further crystal growth.

Comparing GIWAXS patterns (Fig. 2, A and B), the weakened diffraction signal in the initial 60 s suggested that the initial solvated phase of DMSO-DMF-$PbX_2$—in which DMSO is dimethylsulfoxide, DMF is dimethylformamide, and X is a halide ($I^-$, $Br^-$)—was suppressed. This effect could be ascribed to the initial solvated phase isolated by the long-chain β-pV2F molecules (*27*). The intermediate phase concentration was lower in the target than in the control (fig. S14). The scattering feature centered at $q$ = ~10 $nm^{-1}$ along the (001) crystal plane observed in the cast film indicated that the colloid had solidified and converted into a black phase. Notably, we found that the perovskite phase of the target emerged earlier than that of the control ($\Delta t_t > \Delta t_c$), which implied that β-pV2F promoted the conversion of the intermediate phase to the perovskite black phase. The fast phase inversions were

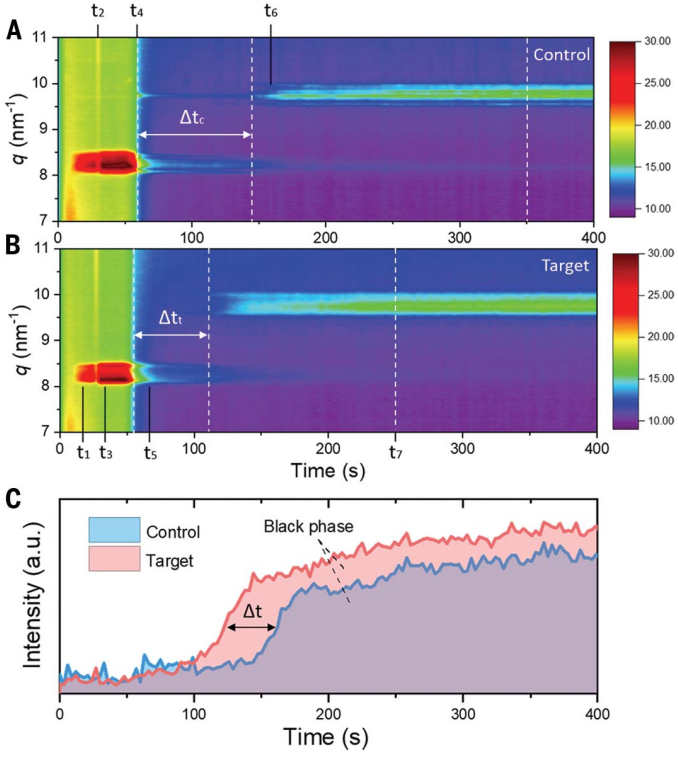


**Fig. 2. Crystallization kinetics of perovskite films.** In situ GIWAXS spectra during forming (**A**) control and (**B**) target perovskite films. (**C**) Time-resolved integrated peak area intensity for black phases of control and target perovskites.

associated with the lower formation energy (*28*, *29*) and could be attributed to β-pV2F rapidly aggregating dispersed $PbX_2$ and organic salts during the elimination of DMSO and DMF (*30*).

Moreover, the target ceased crystal growth sooner at 250 s than the control at 350 s. When the crystallization is completed (stage $t_7$), the signal is more intense in the target than in the control (Fig. 2C). This result indicates that the target perovskite film is more ordered. The time-dependent in situ GIWAXS intensity profiles with other scattering vectors, such as $q$ = ~20 $nm^{-1}$ corresponding to the (002) crystal plane (fig. S15), showed the same phase transition trend. Thus, β-pV2F controls the perovskite crystallization kinetics by lowering the perovskite formation energy, promoting phase conversion, and enabling a more ordered crystal structure (fig. S16).

### Photovoltaic performance

The photovoltaic performance of inverted p-i-n PSCs with control and polymer-modified perovskite films is shown in Fig. 3. The device architecture is glass/indium tin oxide (ITO)/self-assembled [2-(3,6-dimethoxy-9H-carbazol-9-yl)ethyl]phosphonic acid (MeO-2PACz)/perovskite/ [6,6]-phenyl-C61-butyric acid methyl ester ($PC_{61}BM$)/bathocuproine (BCP)/silver (Ag) (fig. S17). Typical current-voltage (*J-V*) curves for the PSCs (Fig. 3A) were measured with a device area of 18 $mm^2$. The control PSCs had a PCE of 22.3%, with short-circuit current density ($J_{sc}$) of 24.7 mA/$cm^2$, $V_{oc}$ of 1.13 V, and fill factor (FF) of 80.2%. With β-pV2F, the device performance improved with a $V_{oc}$ of 1.18 V, a $J_{sc}$ of 24.8 mA/$cm^2$, and a FF of 84.3% for a PCE of 24.6%. The target PSCs' reverse- and forward-sweep *J-V* curves (fig. S18) had negligible hysteresis. A PCE of 24.2% for an aperture area of 9.6 $mm^2$ was obtained from the independent accredited certification institute of Test and Calibration Center of New Energy Device and Module, Shanghai Institute of Microsystem and Information Technology (SIMIT), Chinese Academy of Sciences (fig. S19). We also recorded a PCE of 23.1% for devices with a working area of 1 $cm^2$ (Fig. 3B).

From the external quantum efficiency (EQE) spectra (Fig. 3C), we calculated an integrated $J_{sc}$ of 24.3 and 24.4 mA/$cm^2$ for control and target devices, respectively, comparable to the values extracted from the *J-V* curves. The optical bandgaps of both perovskite absorbers determined by the $x$ axis intercept of the EQE linear are shown in fig. S20 (*31*, *32*). The statistical distribution of the device parameters collected from 38 devices shows an improved PV performance and increased reproducibility with β-pV2F (fig. S21) (*33*), which we explain with better charge extraction and reduced nonradiative recombination (*27*).

The stabilized power outputs at the maximum power point (MPP) are plotted in Fig. 3D. The control device showed a persistent attenuation in efficiency under continuous 1 equivalent sun illumination for 400 s. By contrast, the tracked target device yielded highly stable power output and even progressively improved performance, which we attributed to the light-soaking effect (*34*). The stability of unencapsulated devices under working conditions shows that target PSCs retain 96% of the initial PCE after continuous MPP tracking for 1000 hours. By contrast, control PSCs decay to 84% of their original PCE (Fig. 3E). Device stability statistics ($n$ = 12) are presented in fig. S22. After heating the device to 75°C, 88% PCE was retained in the target device in contrast to only 56% in the control (fig. S23).

We further evaluated device stability against temperature variations. The *J-V* curves in fig. S24 show that the control device's PV parameters ($J_{sc}$, FF, and $V_{oc}$) exhibited large fluctuations when tested at temperatures ranging from −60° to +80°C (table S1). However, this variation was suppressed in the target device (fig. S25 and table S2). Furthermore, compared with the control, the target device had reduced hysteresis and its hysteresis factor was relatively stable under temperature variations (fig. S26). The statistical PCE distribution in Fig. 4, A and B, indicates that the β-pV2F stabilization effect is highly reproducible. All performance parameter evolution is reported in figs. S27 and S28. Subsequently, the unencapsulated devices were aged under rapid thermal cycling (TC) between −60° and +80°C, swept at a rate of 20°C per minute. As shown in Fig. 4, C and D, the control device suffered a severe decline of 75.6% at +80°C and 63.0% at −60°C, whereas



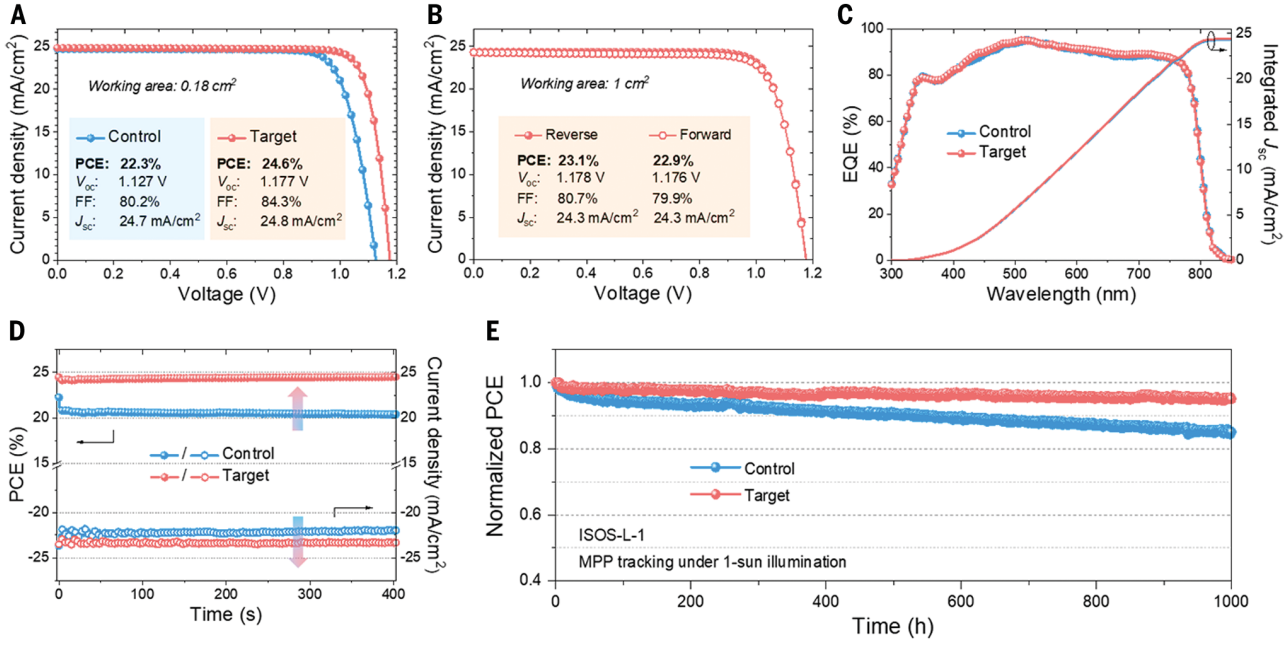


**Fig. 3. PV performance of perovskite solar cells.** (**A**) *J-V* curves of control and target PSCs under a device area of 0.18 $cm^2$. (**B**) *J-V* curves with the reverse and forward sweeps for large-area target PSCs (1 $cm^2$). (**C**) EQE spectra and integrated $J_{sc}$ for control and target PSCs. (**D**) Stabilized power outputs with evolving current density at the maximum power points as a function of time for the best-performing PSCs. (**E**) Long-term stability at maximum power point tracking under room-temperature continuous illumination in $N_2$ atmosphere for unencapsulated PSCs (ISOS-L-1 procedure).

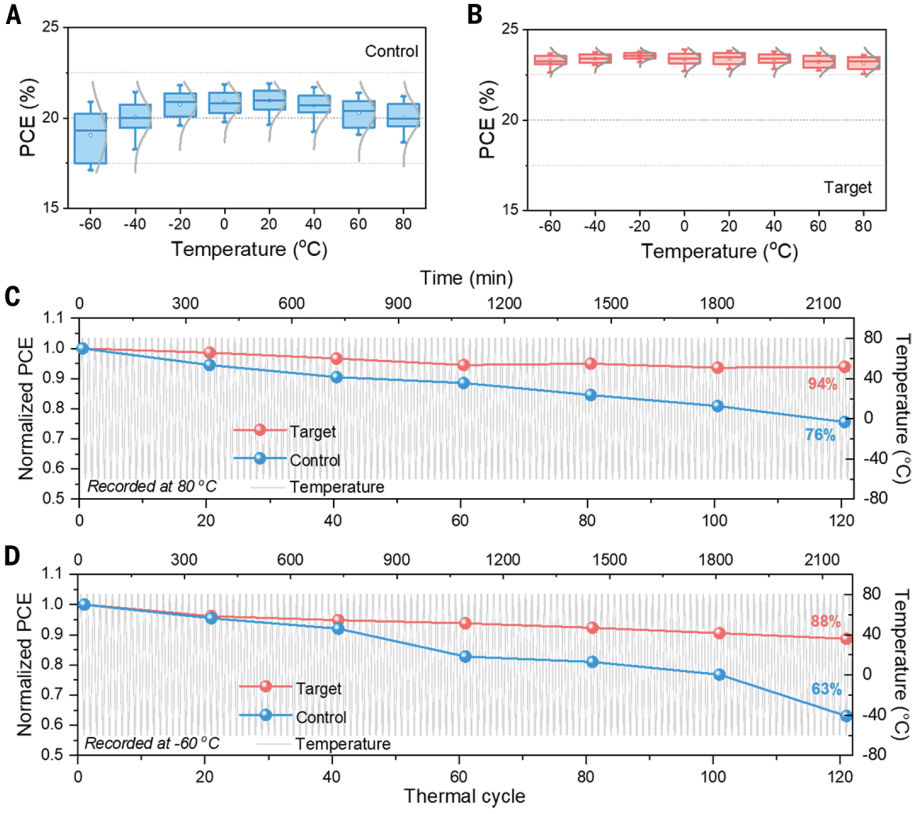


**Fig. 4. Thermal cycling stability of perovskite solar cells.** Statistical temperature dependence PCE profiles of (**A**) control PSCs and (**B**) target PSCs. PCE evolution recorded at (**C**) +80°C and (**D**) −60°C of control and target PSCs against thermal cycles between −60° and +80°C. The rapid thermal cycling was implemented with a ramp rate of 20°C per minute. There is an extra 2-minute waiting window for the device to reach thermal equilibrium when cycling to −60° and +80°C. The temperature starts at room temperature and is heated to +80°C, then cooled to −60°C. The progress ends at room temperature. The time per complete cycle is 18 minutes.

the target device retained 93.9% at 80°C and 88.7% at −60°C of its initial value after 120 thermal cycles.

### Device film morphologies and structures during thermal cycling

The difference in device performance stems from use of β-pV2F in the perovskite film. We characterized the morphology and crystal structure of perovskite films undergoing aging with thermal cycling to identify the impact of β-pV2F. The film aging followed the same device protocol: 120 rapid thermal cycles between −60° and +80°C at a rate of 20°C per minute. As observed from the SEM images in fig. S29, control films exhibited severe morphological degradation with enlarged grain boundaries and voids. Such degradation features were not detected in the aged target films (fig. S30), which appeared nearly identical to the pristine film shown in Fig. 1E. This result indicates that the temperature-induced degradation of perovskite films is suppressed in target perovskites (fig. S31) (*35*).

We observed additional GIWAXS peaks forming in the control perovskite after three thermal cycles (Fig. 5A). Specifically, in the second cycle, the peak for $PbI_2$, a degradation product, emerged at $q$ = 9.2 $nm^{-1}$. During the third thermal cycle, additional peaks ~8.2 and 8.6 $nm^{-1}$ formed, corresponding to the hexagonal photoinactive polytypes 4H and 6H from $Cs_{0.05}(FA_{0.98}MA_{0.02})_{0.95}Pb(I_{0.98}Br_{0.02})_3$ perovskite (fig. S32A) (*36*, *37*). This result indicates that the control perovskite undergoes irreversible phase changes. The generation of these phases may originate from the lattice deformation at the grain boundaries caused by the mutual extrusion of unit cells from neighbored crystals of different orientations (*36*). Such phenomena were not observed in the target perovskite (Fig. 5B), indicating high structural stability (fig. S32B).

For $q$ values from 16 to 19 $nm^{-1}$, we observed additional peaks in both control and target (figs. S33 and S34), corresponding to the tetragonal phase (β phase) (*10*, *38*). The tetragonal phase was only retained in the cold temperature region. This suggests that the degradation products of perovskite under thermal cycling include irreversible $PbI_2$, 4H, and 6H, and reversible tetragonal phase transition, jointly contributing to device performance degradation. Temperature-resolved azimuthally integrated intensity patterns (figs. S35 and S36) indicate that β-pV2F suppresses the phase transitions. We found that suppressing the phase transition also suppressed ion migration in the complete device under working conditions, i.e., lower hysteresis (fig. S37).

Because of differences in thermal expansion coefficients between the perovskite film and the substrate, temperature variation induces strain in the perovskite (*39*, *40*). The control perovskite underwent substantial lattice strain evolution (−0.13 to 0.57%) during thermal cycling (Fig. 5C). We observed that the perovskite strain drifted with temperature cycling, showing a constant lattice parameter change in perovskite. By contrast, the target perovskite exhibits stable strain cycling in a narrower range (−0.06 to 0.38%), corresponding to a recoverable crystal structure and releasable lattice strain (tables S3 to S5). We propose that a strain-buffering and lattice-stabilizing effect exists in target perovskite because β-pV2F creates a self-assembly polymeric layer that coats the crystals within the perovskite film reducing friction during thermal cycling (figs. S38 and S39) (*41*–*44*).

### Conclusions

Thermal stress experienced in normal working conditions induces phase transitions and lattice strains that hamper the stability of perovskite solar cells (PSCs). Coating the crystals comprising the perovskite film with polymer dipoles results in a strain-buffering and lattice-stabilizing effect that mitigates the impact of thermal stress. We selected the specific polymer dipole β-poly(1,1-difluoroethylene) (β-pV2F). The β-pV2F highly ordered dipolar structure interacts with specific perovskite components enabling control of perovskite film crystallization during the processing and energy alignment with the charge-selective contacts within the device. We reported β-pV2F devices

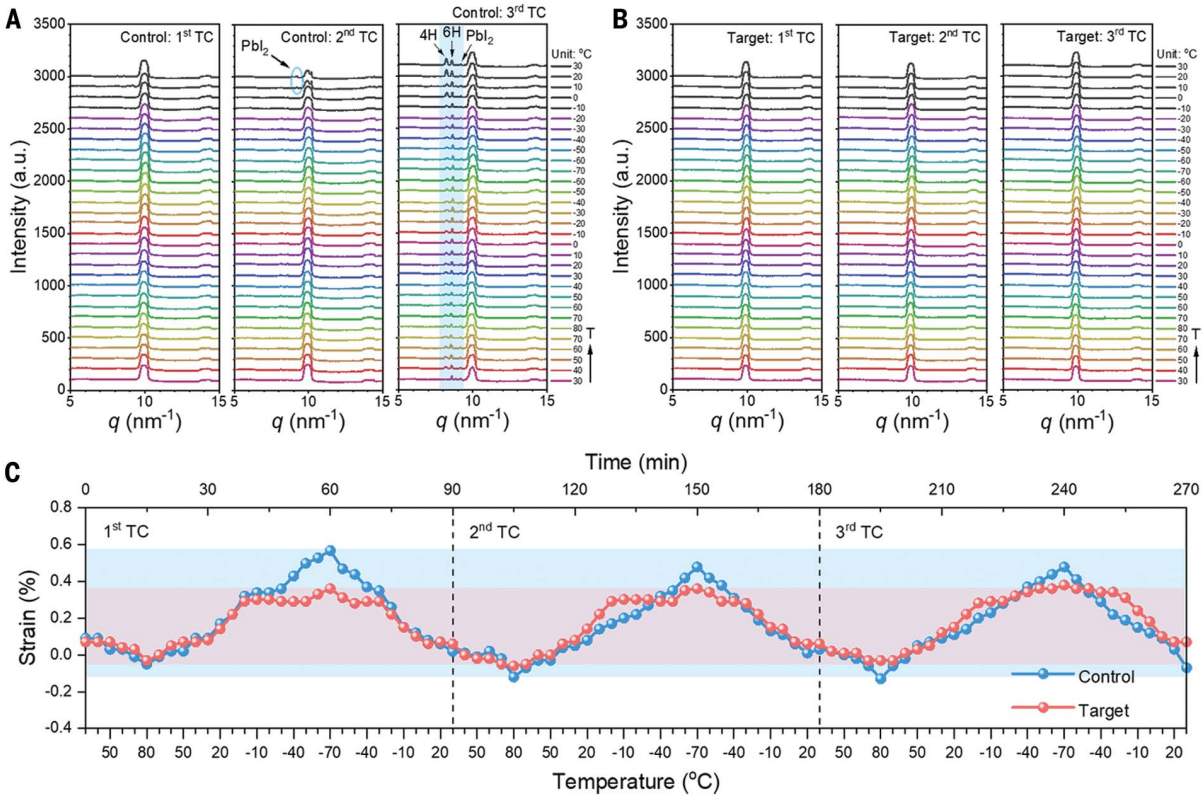


**Fig. 5. Perovskite structural evolution during temperature cycling.** The temperature-resolved GIWAXS profiles for (**A**) control and (**B**) target perovskites. (**C**) The temperature-resolved lattice strain for control and target perovskites. (The temperature starts from room temperature, heating to +80°C and then cooling to −60°C. The progress ends at room temperature. The time per complete cycle is 90 minutes.)

with improved power conversion efficiency up to 24.6% on an active area of 18 $mm^2$ and 23.1% over a larger area of 1 $cm^2$ (certified PCE of 24.24% with an active area of 9.6 $mm^2$ from SIMIT). The β-pV2F strain-buffering effects enabled stable power output at temperatures as high as 75°C and rapid temperature variation between −60° and +80°C. Our work identifies a new strategy for making stable perovskite solar cells.

## REFERENCES AND NOTES


1. The National Renewable Energy Laboratory, US Department of Energy, Office of Energy Efficiency and Renewable Energy, Alliance for Sustainable Energy LLC., Best Research-Cell Efficiency Chart, https://www.nrel.gov/pv/cell-efficiency.html.
2. X. Zheng *et al.*, *Nat. Energy* **5**, 131–140 (2020).
3. Y.-N. Lu *et al.*, *Energy Environ. Sci.* **14**, 4048–4058 (2021).
4. Z. Li *et al.*, *Science* **376**, 416–420 (2022).
5. H. Chen *et al.*, *Nat. Photonics* **16**, 352–358 (2022).
6. X. Li *et al.*, *Science* **375**, 434–437 (2022).
7. M. Degani *et al.*, *Sci. Adv.* **7**, eabj7930 (2021).
8. D. Luo *et al.*, *Science* **360**, 1442–1446 (2018).
9. W. Tress *et al.*, *Nat. Energy* **4**, 568–574 (2019).
10. S. Kahmann *et al.*, *ACS Appl. Mater. Interfaces* **14**, 34253–34261 (2022).
11. X. Zhang, S.-H. Wei, *Phys. Rev. Lett.* **128**, 136401 (2022).
12. D.-J. Xue *et al.*, *Nat. Commun.* **11**, 1514 (2020).
13. R. Cheacharoen *et al.*, *Energy Environ. Sci.* **11**, 144–150 (2018).
14. C. Sun *et al.*, *Nat. Commun.* **12**, 2207 (2021).
15. Z. Wang *et al.*, *Nat. Energy* **2**, 17135 (2017).
16. L. Xu *et al.*, *Adv. Mater.* **34**, 2107111 (2022).
17. L. Canil *et al.*, *Energy Environ. Sci.* **14**, 1429–1438 (2021).
18. A. J. de Jesus Silva, M. M. Contreras, C. R. Nascimento, M. F. da Costa, *Heliyon* **6**, e04573 (2020).
19. P. Metrangolo, L. Canil, A. Abate, G. Terraneo, G. Cavallo, *Angew. Chem. Int. Ed.* **61**, e202114793 (2022).
20. Y. Moriya, R. Ishikawa, S. Akiyama, K. Ueno, H. Shirai, *Chem. Lett.* **49**, 87–90 (2019).
21. J. Jeong *et al.*, *Nature* **592**, 381–385 (2021).
22. G. Li *et al.*, *Adv. Energy Mater.* **11**, 2101539 (2021).
23. D. Koo *et al.*, *Adv. Energy Mater.* **10**, 2001920 (2020).
24. S. Chen *et al.*, *Science* **373**, 902–907 (2021).
25. M. Stolterfoht *et al.*, *Adv. Mater.* **32**, e2000080 (2020).
26. L. Canil *et al.*, *Adv. Energy Mater.* **11**, 2101553 (2021).
27. Y. Li *et al.*, *Joule* **6**, 676–689 (2022).
28. Y. Cho *et al.*, *Adv. Energy Mater.* **8**, 1703392 (2018).
29. H. Hu *et al.*, *J. Mater. Chem. A Mater. Energy Sustain.* **8**, 1578–1603 (2020).
30. M. Qin *et al.*, *Adv. Mater.* **32**, e2004630 (2020).
31. A. Y. Alsalloum *et al.*, *Energy Environ. Sci.* **14**, 2263–2268 (2021).
32. P. S. C. Schulze *et al.*, *Sol. RRL* **4**, 2000152 (2020).
33. R. Azmi *et al.*, *Science* **376**, 73–77 (2022).
34. S. Wu *et al.*, *Joule* **4**, 1248–1262 (2020).
35. Z. Dai *et al.*, *Science* **372**, 618–622 (2021).
36. M. Qin *et al.*, *Adv. Mater.* **31**, e1901284 (2019).
37. P. Gratia *et al.*, *ACS Energy Lett.* **2**, 2686–2693 (2017).
38. W. Peng *et al.*, *Angew. Chem. Int. Ed.* **55**, 10686–10690 (2016).
39. C. Zhu *et al.*, *Nat. Commun.* **10**, 815 (2019).
40. J. Zhao *et al.*, *Sci. Adv.* **3**, eaao5616 (2017).
41. L. Wang, Q. Gong, S. Zhan, L. Jiang, Y. Zheng, *Adv. Mater.* **28**, 7729–7735 (2016).
42. L. T. Hieu, S. So, I. T. Kim, J. Hur, *Chem. Eng. J.* **411**, 128584 (2021).
43. W. Chen *et al.*, *Adv. Funct. Mater.* **29**, 1808855 (2019).
44. L. Zuo *et al.*, *Sci. Adv.* **3**, e1700106 (2017).


## ACKNOWLEDGMENTS

The authors acknowledge the support of all the technicians at Helmholtz-Zentrum Berlin (HZB). The authors thank beamline BL14B1 at the Shanghai Synchrotron Radiation Facility (SSRF) for providing the beam time. G.L., L.C., and M.H.A. thank the support from HyPerCells graduate school at HZB. R.Z. was supported by the National Natural Science Foundation of China (22103022). G.L. thanks the Chinese Scholarship Council (CSC) for its financial support (201906150131). M.S. and W.Z. thank the German Research Foundation (DFG) for funding (SPP2196, 431314977/GRK 2642). M.S. acknowledges funding by ProperPhotoMile. Project ProperPhotoMile is supported under the umbrella of SOLAR-ERA.NET Cofund 2 by the Spanish Ministry of Science and Education and the AEI under the project PCI2020-112185 and CDTI project number IDI-20210171; the Federal Ministry for Economic Affairs and Energy based on a decision by the German Bundestag project number FKZ 03EE1070B and FKZ 03EE1070A and the Israel Ministry of Energy with project number 220-11-031. The European Commission supports SOLAR-ERA.NET within the EU Framework Programme for Research and Innovation HORIZON 2020 (Cofund ERA-NET Action, 786483). This work has received funding from the European Research Council (ERC) under the European Union's Horizon 2020 research and innovation programme (grant agreement 804519). **Author contributions:** G.L., L.W., M.L., and A.A. conceived the idea. G.L. and M.L. designed the experiments. G.L., Z.S., L.W., S.T., M.H.M., Z.Z., F.Y., and M.L. fabricated and characterized perovskite films and devices. Z.S. and C.W. conducted the GIWAXS measurements. G.L., D.H., L.W., W.Z., R.Z., F.Y., Y.J., and M.L. performed the device performance measurements. G.L., Z.S., L.C., L.W., M.L., and A.A. participated in the data analysis and result discussions. G.L. composed the manuscript. D.H., M.H.M., J.D., S.T., W.Z., J.J.J.-R., M.M.B., G.N., B.N., M.L., and A.A. contributed to suggestions for

the manuscript. L.W., W.C.T., Z.L., X.G., Z.W., E.U., M.S., M.L., and A.A. provided expertise and supervised the work. All authors reviewed the manuscript. **Competing interests:** Authors declare that they have no competing interests. **Data and materials availability:** All data are available in the manuscript or the supplementary materials. **License information:** Copyright © 2023 the authors, some rights reserved; exclusive licensee American Association for the Advancement of Science. No claim to original US government works. https://www.sciencemag.org/about/science-licenses-journal-article-reuse

## SUPPLEMENTARY MATERIALS

science.org/doi/10.1126/science.add7331
Materials and Methods
Supplementary Text
Figs. S1 to S39
Tables S1 to S5
References (*45*–*52*)

Submitted 30 June 2022; accepted 27 December 2022
10.1126/science.add7331

# Highly efficient p-i-n perovskite solar cells that endure temperature variations

Guixiang Li, Zhenhuang Su, Laura Canil, Declan Hughes, Mahmoud H. Aldamasy, Janardan Dagar, Sergei Trofimov, Luyao Wang, Weiwei Zuo, José J. Jerónimo-Rendon, Mahdi Malekshahi Byranvand, Chenyue Wang, Rui Zhu, Zuhong Zhang, Feng Yang, Giuseppe Nasti, Boris Naydenov, Wing C. Tsoi, Zhe Li, Xingyu Gao, Zhaokui Wang, Yu Jia, Eva Unger, Michael Saliba, Meng Li, and Antonio Abate

*Science* **379** (6630), . DOI: 10.1126/science.add7331

**Running hot and cold**

Like other solar cells, commercial perovskite solar cells (PSCs) would not only need to maintain operation at the high temperatures generated in direct sunlight but also endure the lattice strain created by temperature changes throughout the year. Li *et al*. fabricated high-quality perovskite crystalline films by adding a fluorinated polymer, the dipoles of which lowered formation energy of the perovskite black phase, decreased defect density, and also tuned the surface work function for charge extraction. Power conversion efficiencies of 23% were achieved for 1-square-centimeter devices that retained over 90% of their efficiency after testing conditions for 3000 hours and after repeated cycling between -60° and 80°C. —PDS







*Science* (ISSN 1095-9203) is published by the American Association for the Advancement of Science. 1200 New York Avenue NW, Washington, DC 20005. The title *Science* is a registered trademark of AAAS.